

# Natural analogs for improved understanding of coupled processes in engineered earth systems: examples from karst system evolution

Harihar Rajaram\*, Wendy Cheung and Abhijit Chaudhuri

Department of Civil Environmental and Architectural Engineering, University of Colorado, Boulder, CO 80309-0428, USA

There is an increasing need to understand the behaviour of engineered earth systems, from the viewpoint of safe waste disposal and exploration of renewable energy sources. Often, human activities lead to significant perturbations of the earth systems, involving hydrologic, mechanical, thermal and chemical processes. Prediction of the long-term response of earth systems to large perturbations is critical for evaluating their design, performance and operation. Because many of the processes involved in system response will manifest over decades or centuries, field-testing during the design stage is infeasible. In this connection, we propose that development of coupled process simulators and testing them on natural analogs provided by geologic systems may be fruitful. As example, we illustrate our attempts to simulate the development of two types of cave systems – branchwork in meteoric environments and mazework in hypogene or hydrothermal environments. Our computational models combine hydraulic, thermal and chemical processes in limestone fractures and consider the influence of subsurface heterogeneity as well. Our computational results vividly demonstrate the mechanisms by which branchwork patterns develop in meteoric environments and demonstrate how sustained dissolution along upward flow channels can be established in hypogene environments, thus creating favourable conditions for development of maze patterns. Investigations of system sensitivities in both types of environments indicate that a surprisingly robust pattern of behaviour results, thus serving as a target for developing simplified conceptual models of these systems. We also discuss the implications of our results for design, operation and risk analysis of engineered earth systems.

**Keywords:** Engineering earth systems, karst system evolution, natural analogs.

## Introduction

THE increased energy demands of the industrial societies of the 20th century prompted the exploration of alterna-

tive energy sources, including nuclear energy, geothermal, wind, tidal and wave energy. In the case of nuclear energy, safe disposal of radioactive waste generated in the fuel cycle emerged as an important need, prompting the concept of subsurface or geological waste repositories<sup>1</sup>. At the same time, consumption of fossil fuels has increased significantly, leading to increased emission of carbon dioxide that is implicated in the recently documented warming climate<sup>2</sup>. Recent efforts have focused on reducing carbon dioxide input to the atmosphere by subsurface storage of fossil power plant emissions<sup>3</sup>. Since the 1960s, geothermal heat has been viewed as a promising source of renewable energy<sup>4</sup>, and the design and operation of geothermal power plants remains an active area of research<sup>5</sup>. All the above activities involve an interaction between engineered and natural systems. They require a refined understanding of the long-term response of subsurface environments to significant perturbations, involving several coupled processes, including evolution of flow/thermal regimes, deformation (and perhaps even fracturing), and geochemical alteration of medium properties by precipitation/dissolution reactions.

Coupled process (thermo-hydro-mechano-chemical) simulation has been in development for the last 20 years<sup>6,7</sup>, and advanced in step with the dramatic advances in computational technology during the same period. Today, the term ‘multi-physics’ is more commonly used to describe such problems. Both the complications resulting from nonlinear coupled processes and the inherent heterogeneity of natural subsurface environments pose significant computational challenges. The impacts of nuclear waste disposal and subsurface carbon storage will only be evident a few hundred years after disposal/storage operations commence. Thus, it is practically impossible to validate coupled process simulators for evaluating the long-term impacts of these operations. Although short-term tests have been conducted, the wide separation in time scales between deformation (fast), thermal and geochemical (very slow) processes preclude full evaluation of slower processes in these tests. Natural analogs in geological systems, where interacting coupled processes are manifest in nature over very long time scales are promising in this context. Examples of such natural analogs include: karst and cave systems<sup>8,9</sup>, organized cementa-

\*For correspondence. (e-mail: hari@colorado.edu)

tion/precipitation patterns<sup>10</sup>, systematic quasi-periodicity in geysers and hydrothermal systems<sup>11</sup>, and low-level natural seismicity<sup>12</sup>. In several of these systems, self-organized interactions between the coupled processes lead to distinctly vivid patterns/features (e.g. cave shapes, quasi-periodicity of geyser eruptions) that dominate their overall behaviour. Thus these systems also serve as case studies for evaluating the sensitivity of dominant behaviours to various levels of computational model complexity and resolution, facilitating the identification of minimum model requirements for predicting dominant or 'first-order' aspects of both natural and engineered system behaviour.

Motivated by the above considerations, the present article presents some of our efforts to reproduce shape patterns observed in cave systems using coupled process models. Palmer<sup>8</sup> and Ford and Williams<sup>9</sup> have presented classifications of major karst and cave systems in limestone based on their shape patterns (morphology), along with hypotheses relating their morphology to the environment in which they developed. We focus on two specific types of cave morphologies – 'branchwork' (river network type shapes) that typically originates in meteoric (i.e. shallow recharge) environments, and 'mazework' that originates in various environments, notably in the up-flow zones of hydrothermal flow systems, also referred to as hypogene (i.e. water rising from significant depth) systems. Our computational models incorporate coupling between fluid flow, solute transport, dissolution, fracture enlargement, permeability alteration, and in the hypogene case, also include heat transfer in fractures and the surrounding rock mass. We evaluate the basic ingredients necessary for reproducing the morphology of branchwork and mazework cave systems. We must note that even in this era of high-performance computing, three-dimensional simulations in fracture networks are a bit prohibitive and we largely consider the development of shape patterns within a single fracture or fault plane.

In this article, we first present the flow and transport equations required for modelling karst evolution. We then present computational results from our efforts to model meteoric and hypogene karst evolution. We conclude with a discussion of the insights gained from modelling karst evolution and their relevance to engineered earth system.

## Flow and transport equations

Our approach to modelling the evolution of karst systems is based on aperture-averaged two-dimensional flow and transport equations for variable-aperture fractures. Flow and heat transport in the rock matrix adjacent to the fracture are neglected in the meteoric case, but included in the formulation for the hypogene case. For reference, we define a coordinate system where the fracture is in the  $x$ - $z$  plane and the  $y$ -direction is perpendicular to the fracture

with its origin on the mid-plane of the fracture. The aperture-averaged flow equation in the fracture is:

$$\frac{\partial(\rho b)}{\partial t} + \nabla \cdot (\rho \mathbf{q}) = \sum \pm \rho v_y|_{y=\pm b/2}, \quad (1)$$

where  $\rho$  is the fluid density,  $b$  the local fracture aperture,  $\mathbf{q}$  the aperture-integrated flux vector in the fracture plane ( $x$ - $z$ ). On the right-hand side,  $\sum \pm \rho v_y|_{y=\pm b/2}$  represents the flux across the two interfaces between the fracture and rock matrix (+ for inflow into the fracture), which is only considered in the hypogene case. The two-dimensional flux vector in the fracture is defined as:

$$\mathbf{q} = -\frac{b^3}{12\mu} f(\text{Re}) [\nabla p - \rho \mathbf{g}], \quad (2)$$

where  $p$  denotes the fluid pressure,  $\mathbf{g}$  denotes gravitational acceleration (vector),  $\mu$  is the dynamic viscosity of the fluid and  $f(\text{Re})$  represents the influence of turbulent flow resistance, via the Reynolds number,  $\text{Re}$ , as explained further below. At low Reynolds numbers,  $f(\text{Re}) = 1$  and eq. (2) reduces to the well-known local cubic law.

In general, transport and dissolution of calcite in karst systems is a multi-component reactive transport problem. Andre and Rajaram<sup>13</sup> showed that under closed-system conditions representative of the early stages of karstification (i.e. under fully saturated flow conditions) the multi-component reactive transport problem can be reformulated to involve a single transport equation (for  $\text{Ca}^{2+}$ ), which however requires speciation calculations in the calcium carbonate system to compute dissolution rates. Alternatively, several previous works use an empirical rate equation for calcite dissolution involving only the concentration of  $\text{Ca}^{2+}$  ions<sup>8,14</sup>. The aperture-averaged effective transport equation for  $\text{Ca}^{2+}$  (whose concentration in molal units is denoted by  $C$  below) can be represented as:

$$\frac{\partial(\rho b C)}{\partial t} + \nabla \cdot (\rho \mathbf{q} C) - \nabla \cdot (\rho \mathbf{D} \cdot \nabla C) = R_C. \quad (3)$$

In eq. (3),  $\mathbf{D}$  denotes the diffusion–dispersion tensor for aperture-averaged transport. Chaudhuri *et al.*<sup>15</sup> presented a dimensional analysis to show that the diffusion–dispersion term may be neglected in comparison with the advection and reaction terms in most realistic situations. The term  $R_C$  denotes the wall flux of  $\text{Ca}^{2+}$  in moles/m<sup>2</sup>/s (dissolution rate plus the contribution from fracture-matrix exchange; the latter is only relevant in the hypogene case). The dissolution rate can be computed by incorporating the influence of surface reaction, diffusion across the aperture, and gradients in solubility associated with temperature (and/or pressure gradients). The specific forms of  $R_C$  used in the meteoric and hydrothermal case simulations are described below.

The heat transport equation in the fracture is used only in the hypogene case (the meteoric system is assumed to be isothermal), and is given by:

$$\frac{\partial(\rho b C_p T)}{\partial t} + \nabla \cdot (\rho \mathbf{q} h) - \nabla \cdot (\lambda b \cdot \nabla T) = \sum \pm \left( \rho \nu_y h_r - \lambda_r \frac{\partial T_r}{\partial y} \right) \Big|_{y=\pm b/2} \quad (4)$$

In eq. (4),  $T$  denotes the aperture-averaged water temperature in the fracture,  $C_p$  the specific heat of water,  $h$  the enthalpy of water in the fracture,  $\lambda$  the thermal conductivity of water,  $h_r$  the enthalpy of water in the rock matrix,  $\lambda_r$  the thermal conductivity of the surrounding rock, and  $T_r$  the temperature in the rock. The right-hand side of eq. (4) represents the thermal exchange between the fracture and the rock (positive for inward heat flux), which incorporates both advective and conductive exchange.

Alteration of the fracture aperture is computed based on a mass balance of rock at the fracture walls, as follows:

$$\frac{\partial b}{\partial t} = \frac{R_C}{\omega \rho_r} \quad (5)$$

In eq. (5),  $\omega$  is the number of moles of  $\text{Ca}^{2+}$  per unit mass of rock (calcite) and  $\rho_r$  is the rock density. It should be noted that the right hand side of eq. (5) scales as  $C_s/(\omega \rho_r)$ , which is very small (order of  $10^{-5}$ ), implying that the rate of aperture growth is very small. This feature may be exploited to treat the flow and  $\text{Ca}^{2+}$  transport equations as quasi-steady state equations in the meteoric case<sup>16</sup>, or explicitly couple aperture alteration to implicit formulations of the coupled fluid flow and heat transfer equations in the hydrothermal case<sup>17</sup>. The next two sections describe additional features of the governing equations, computational approaches and results for the meteoric and hydrothermal problems.

## Meteoric case simulations

Previous work has focused on the development of meteoric cave systems in fracture networks<sup>18-22</sup> and outlined factors controlling karstification rates and the morphology of meteoric cave systems. We consider variable-aperture fractures in limestone that correspond to bedding plane partitions or extensive fractures. Palmer<sup>8</sup> notes that a very large fraction of the total length of cave passages in a sample including about 500 caves are guided by favourable beds or bedding plane partitions, wherein the cave passages are often curvilinear. Although Hanna and Rajaram<sup>16</sup> previously examined karstification in variable-aperture fractures, they did not consider the behaviour after the onset of turbulent flow or demonstrate the development of branchwork patterns. The goal of our simulations is to understand how branchwork patterns develop from flow in single fracture planes in meteoric karst sys-

tems. In this case, we assume isothermal conditions at a temperature of 15°C, so that there is no need to model the temperature field (eq. (4)).

## Additional specifications for flow and transport equations

For the meteoric case, we used the following representation of the influence of turbulent resistance, modified from Louis<sup>23</sup>, which reduces the fracture transmissivity above a Reynolds number of 2300.

$$f(\text{Re}) = 1, \text{Re} < 2300; \quad f(\text{Re}) = \frac{332}{\text{Re}^{3/4}}, \text{Re} > 2300. \quad (6)$$

Sensitivity analyses<sup>24</sup> did not reveal significant changes in the evolution of the fracture aperture field when alternative turbulent resistance equations were used. The wall flux term  $R_C$  in eq. (4) is represented as the smaller of a surface reaction rate ( $R_{C,\text{surface}}$ ) and a diffusion-controlled rate ( $R_{C,\text{diff}}$ ), which are calculated as described below. The surface-reaction rate is defined by:

$$R_{C,\text{surface}} = k \left( 1 - \frac{C}{C_s} \right)^n, \quad (7)$$

where  $C_s$  is the calcium ion concentration corresponding to the solubility limit. At 15°C, a partial pressure  $p\text{CO}_2 = 0.003$  atm at the entrance to the fracture, and closed system conditions within the fracture,  $C_s = 1.768 \times 10^{-4}$  moles/litre. The rate parameters in eq. (7) suggested by Dreybrodt<sup>14</sup> are:

$$k = 0.015 \text{ moles/m}^2/\text{s}; n = 2.2 \text{ for } C/C_s < 0.7, \\ k = 0.131 \text{ moles/m}^2/\text{s}; n = 4.0 \text{ for } C/C_s > 0.7. \quad (8)$$

The change in reaction order from 2.2 to 4 at a saturation index of 0.7 (ref. 14) is the so-called kinetic trigger that reduces the dissolution rate as the saturation or equilibrium concentration is approached. It is believed to permit reasonable dissolution rates to persist deep inside a karst flow path and enable cave development over (geologically) reasonable durations.

The diffusion-limited dissolution rate is computed from:

$$R_{C,\text{diff}} = h_m (C_s - C), \quad (9)$$

where  $h_m$  is the mass transfer coefficient, given by:

$$h_m = \frac{\text{Sh}_d D_m}{2b}; \quad \text{Sh}_d = 8.24 \quad (\text{laminar}), \\ \text{Sh}_d = \frac{(f/8)(\text{Re} - 1000)\text{Sc}}{1 + 12.7(f/8)^{1/2}(\text{Sc}^{2/3} - 1)} \quad (\text{turbulent}). \quad (10)$$

In eq. (6),  $D_m$  is the molecular diffusion for  $\text{Ca}^{2+}$  in water and  $\text{Sh}_d$  the Sherwood number. For laminar flow, a value of  $\text{Sh}_d = 8.24$ , corresponding to a wide rectangular duct<sup>25</sup> was used. For turbulent flow, the Gnielinski relationship<sup>26</sup> (after Howard and Groves<sup>27</sup>) was used, where  $\text{Re}$  is the Reynolds number,  $\text{Sc}$  is the Schmidt number and  $f$  is the friction factor for hydraulically smooth flow, given by the Blasius relationship  $f = 0.316/\text{Re}^{0.25}$ . Flow and calcite transport in the rock matrix are neglected in the analysis of the meteoric karst evolution, which is consistent with most of the previous work. As noted above, heat transport in either the fracture or matrix is not considered in the analysis of meteoric karst evolution.

### Computational results

Here, we present qualitative and quantitative results to document the process of dissolution growth, increase in effective transmissivity and emergence of the branchwork pattern. The initial log-aperture field is a realization of a stationary Gaussian random field with an isotropic exponential correlation function (correlation length = 1 m). A mean aperture ( $\mu$ ) of 0.22 mm and different values of the coefficient of variation ( $\sigma/\mu$ ) of the aperture field were considered. The results presented in this section are based on simulations in fractures with  $51.2 \times 51.2$  m in-plane dimensions, and a computational grid of  $0.1 \times 0.1$  m. Cheung<sup>24</sup> also presented simulations in a domain four times larger and confirmed that the behaviour is similar to that presented here. The boundary conditions involve a mean flow driven by a constant hydraulic gradient, imposed across two parallel sides of the fracture, with no-flux boundaries on the two perpendicular boundaries. On the inflow boundary, water enters the fracture with no dissolved calcite. In the early stages of meteoric karst evolution, the transmissivity is low and the assumption of a constant hydraulic gradient is reasonable<sup>8,9</sup>. The fracture orientation may be considered arbitrary, although constant head boundary conditions are most realistic when we consider a mildly inclined bedding plane.

We begin by presenting a sequence of aperture, head, flux and dissolution rate fields (Figure 1 *a* and *b*) for one realization of a variable aperture fracture with  $\sigma/\mu = 0.5$ . The evolution of the entrance flux with time is shown in Figure 2 for this simulation. The columns in Figure 1 *a* and *b* show the aperture, head, flux vector magnitude and dissolution rate fields within the fracture at various times. The preferential flow paths resulting from initial aperture variability are evident in the flux field at  $t = 0.5$  years. The corresponding dissolution rate field shows very low dissolution rates in the interior of the domain, because the  $\text{Ca}^{2+}$  concentration builds up to saturation farther into streamlines. Near the entrance, there are 'fingered' regions of high dissolution rates, which are associated with the preferential flow paths (see the corresponding flux

magnitude field) or equivalently, locations of peaks in the entrance flux (see Figure 2). Some of these regions develop into dissolution fingers, as seen in the second row of Figure 1 *a* ( $t = 10$  years). Although many dissolution fingers are initiated, some of them cease to grow beyond a point. At  $t = 10$  and 25 years, five dissolution fingers are continuing to grow. Interspersed between these five fingers are several relict fingers, which have evidently stopped growing.

The head fields at  $t = 10$  and 25 years show a flat region with little head drop from the entrance of the fracture to the tips of the fingers. This is because the aperture within the dissolution fingers is substantially larger than outside the fingers, and the overall effective transmissivity near the entrance is increased as a result. The head surface is flat not only within the fingers, but also in a 'region of influence' surrounding them, which extends across the whole width of the fracture near the entrance, and becomes wavy around the finger tips. Correspondingly, the flux fields and entrance flux (Figure 2) show that the flow is discharged from the entrance largely through the fingers, even though flow initially entered at comparable rates across the entire fracture ( $t = 0.5$  years). The dissolution rate fields (note that these fields are displayed using a nonlinear grey scale) at  $t = 10$  and 25 years show that high dissolution rates occur largely in the dissolution fingers and at the finger tips and that the dissolution rate outside the fingers is orders of magnitude smaller. This is because the large flux within the fingers leads to low concentrations and thus larger dissolution rates. Because of the large apertures, the dissolution rate within the fingers is mostly determined by the diffusion-limited rate (eq. (9)) rather than the surface-reaction limited rate (eq. (7)).

The locations of the four prominent fingers do not directly correspond to the four largest peaks in the initial entrance flux. Rather, a preferred spacing develops between the fingers. Two fingers that are very close will compete with each other and only one of them will propagate beyond a point. However, another finger that is some distance away, and hence outside the 'region of influence' of the first finger can grow independently until their regions of influence begin to overlap and they begin to compete. The reason for this behaviour is clarified in plots of the head field at  $t = 10$  and 25 years. The important point is that the head surface is flat in a 'region of influence' surrounding fingers, which extends across the whole width of the fracture near the entrance, and becomes wavy around the finger tips. The width of the undulations in the flat portion of the head surface surrounding a finger become wider as the finger advances down-gradient. Thus 'nearby' fingers (e.g. the third prominent finger from the top, which has stopped growing at 25 years) that are within the 'region of influence' of a finger that has advanced further (e.g. the fourth prominent finger from the top at 25 years) will not be



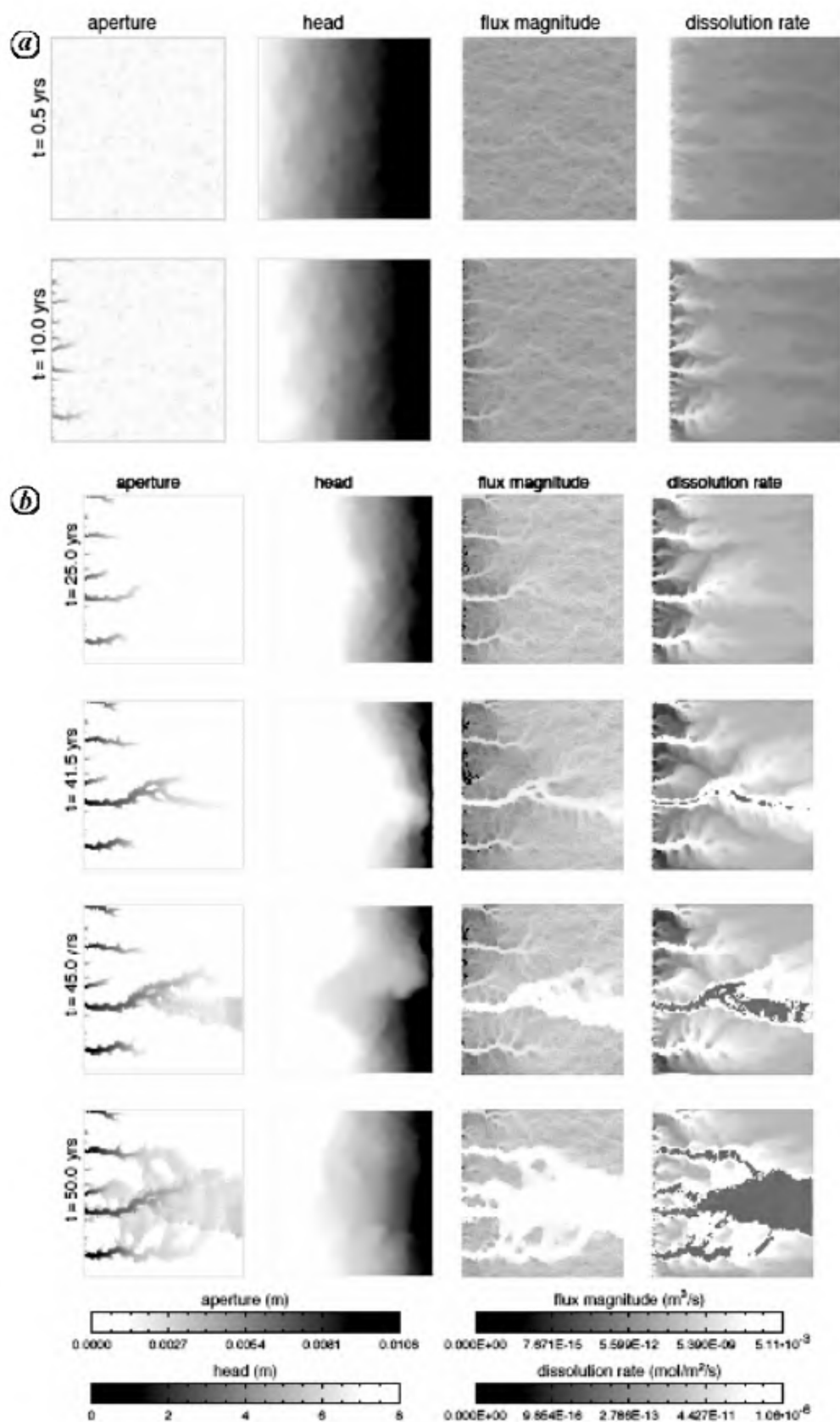


**Figure 1.** *a*, Evolution of aperture, head, flux magnitude and dissolution rate fields for base-case meteoric karst evolution simulation (the coefficient of variation of the aperture field,  $\sigma/\mu = 0.5$ ). *b*, Base-case meteoric karst simulation at later times. The legends describe the gray scales used in the plots.

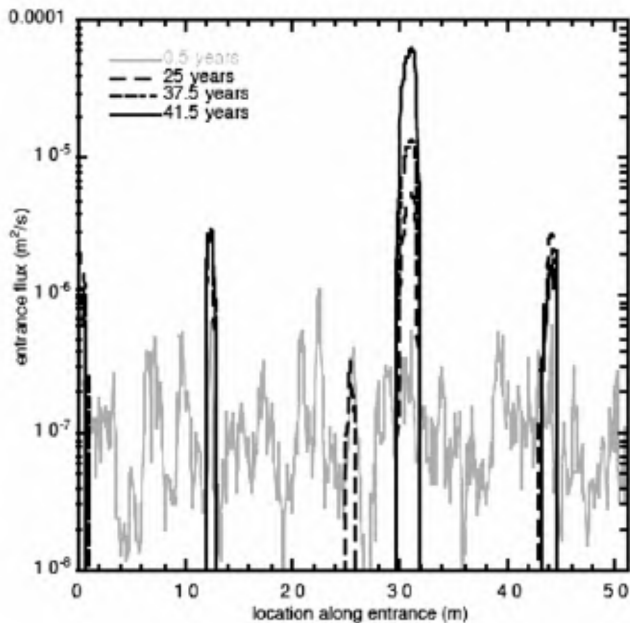


**Figure 2.** Evolution of entrance flux into the fracture for the base-case meteoric karst evolution simulation corresponding to Figure 1 *a, b*. Note that for  $t > 25$  years, the flux outside the fingers is smaller than  $10^{-8} \text{ m}^2/\text{s}$ . Also note that only the flux in the dominant finger is increasing with time. The finger to its immediate left carries almost no flux in the plots after 25 years.

able to discharge much flow because of the flat hydraulic gradient at their tips.

As time progresses, the finger which has advanced farthest downstream typically grows at the fastest rate, because it has the largest head gradient between its tip and the downstream boundary, and hence is able to discharge the most flow. There is also an element of positive feedback involved in this process, in that the rate of advancement of the dominant finger accelerates and far exceeds those of the others. One dominant finger thus ‘breaks through’ the domain (41.5 years), leaving the other fingers significantly behind. The flux field at breakthrough shows a very large flow rate within the dominant finger, with smaller flows in the other subdominant fingers. Figure 2 shows that the flow rates into the subdominant fingers is about one-fifth of that in the dominant finger. Furthermore, the flux entering the subdominant fingers either decreases with time or remains constant, causing very little growth between 25 and 41.5 years. Similar behaviour was observed in the experimental studies of Ewers<sup>28</sup> and explained by Ford and Williams<sup>9</sup>. However, in the experiments of Ewers<sup>28</sup>, the locations of the fingers were determined by the locations of the regularly spaced injection ports. In variable-aperture fractures, an apparent regularity in the spacing between fingers arises naturally as a result of the aforementioned influence of growing fingers on the head and flux fields within the fracture and in other fingers. The development of systematic spacing between dissolution

fingers has been described previously by Cheung<sup>24</sup>, Cheung and Rajaram<sup>29</sup> and Scymzak and Ladd<sup>30</sup>.

We define the breakthrough time as the time at which turbulent flow is first encountered anywhere in the domain (typically within the dominant finger), which also coincides with a dramatic increase in the flux through the dominant finger, and its arrival at the outflow boundary. In the early stages of turbulent flow, there is a strong divergent flow from the tip of the dominant finger to the downstream boundary, which leads to a flared growth pattern ( $t = 45$  years). The dissolution rate field at breakthrough shows low dissolution rates in the central portion of the dominant finger. These regions reflect the onset of turbulent flow within the core of the dominant finger. Because the diffusion-limited rate is now controlled by turbulent diffusion, which leads to a much larger mass transfer rate, concentrations build up quickly and the dissolution rate reduces. However, high dissolution rates continue to persist at the lateral fringes of the dominant finger and in wider portions of the dominant channel, where the local flux is lower, promoting widening of the channel. Shortly after turbulent flow appears in the dominant finger, there is a dramatic change in the behaviour of the head field ( $t = 45$  years). Within the dominant finger, turbulent resistance leads to significant head losses, while the head in the surrounding regions (especially the subdominant fingers) behaves as in the laminar flow regime. As a result, significant head gradients are established between the tips of the subdominant fingers and the sides of the dominant finger. The subdominant fingers now grow towards the dominant finger and eventually coalesce with it. This behaviour is evident in the last two aperture fields in Figure 1 *b*. The pattern of dissolution growth seen in the last two aperture fields is clearly suggestive of a branchwork structure. Some anastomotic (loop) structures are contained within the overall branchwork. With time, flow in the subdominant fingers also becomes turbulent, and the head surface is no longer flat in the upstream portion of the fracture. These simulations were terminated when half the cells in the domain had become encroached by turbulent flow, and the last set of aperture, head, flux and dissolution rate fields correspond to the end of the simulation. It may be expected that if the simulation were continued, the entire fracture would experience turbulent flow, and aperture growth will occur throughout the entire fracture at a slow rate, as opposed to the rapid selective growth during the laminar flow regime. However, hydrology imposes a limit to the amount of flow that can be discharged through the fracture and a branchwork pattern will remain in place in nature, because the flux through the bedding plane cannot exceed hydrologic inputs. Cheung<sup>24</sup> presented numerical simulations with an upper bound on the flux and confirmed that a branchwork remains in place for a very long duration under these conditions, with continuing growth within the branchwork. In nature, the above competition between growing

dissolution fingers may also be played out in a multiscale sense over a hierarchy of flow systems and sub-systems, and will also be influenced by the discrete nature of inputs from sinkholes.

Next, we briefly discuss the behaviour in fractures with two different values of  $\sigma/\mu$ , 0.1 and 1.0. The same realization of the random field used in the earlier simulation (Figure 1) was rescaled to obtain initial aperture fields with different values of  $\sigma/\mu$ , while maintaining the same hydraulic aperture (in other words, the geometric mean aperture or mean of log aperture was maintained the same in all cases), to enable a comparison between fractures that are initially hydraulically equivalent. Figure 3 shows the aperture, head, flux vector magnitude and dissolution rate fields for  $\sigma/\mu = 1.0$  and 0.1, at three times – before breakthrough, at breakthrough and at the end of the simulation. The  $\sigma/\mu = 1$  case behaves very much like the  $\sigma/\mu = 0.5$  case, except that the subdominant fingers are suppressed to a larger extent. In particular, the second finger from the top is suppressed by the upward orientation of the two fingers below it, which interfere with its growth. Cheung and Rajaram<sup>29</sup> also documented this type of behaviour for larger values of  $\sigma/\mu$ . The flux fields reveal a larger degree of channelling downstream of the fingers, as is to be expected with an increased degree of heterogeneity. The behaviour after turbulent flow is initiated in the  $\sigma/\mu = 1$  case, is also largely similar to that in the  $\sigma/\mu = 0.5$  case.

In the relatively less heterogeneous  $\sigma/\mu = 0.1$  case, the behaviour is somewhat different from that of other two cases. The dissolution fingers are more linear and exhibit very little branching during the initial growth phase. The subdominant channels are not inhibited to the extent that they are in the  $\sigma/\mu = 0.5$  case, largely because of the linear growth and absence of branching, which ensures that fingers do not interfere with the growth of other fingers unless they are very close. It is interesting to note that the regularity in the spacing between the fingers in the  $\sigma/\mu = 0.1$  case is much more striking than in the other cases. This feature again results from the behaviour of the head field associated with the high transmissivity within fingers, as discussed previously. The flow fields at the tip of the fingers in the  $\sigma/\mu = 0.1$  case, are similar to flows emanating from a high-transmissivity slot in a homogeneous transmissivity field<sup>29</sup>. It is also interesting to note that due to the reduced degree of heterogeneity, the finger that was dominant in the  $\sigma/\mu = 0.5$  and 1.0 cases is no longer dominant in this case; the finger at the upper boundary breaks through first. Shortly thereafter, another finger breaks through. Both these fingers are then joined by nearby fingers that grow towards them in the turbulent flow regime. It is interesting to note that in the mildly heterogeneous  $\sigma/\mu = 0.1$ , there is greater chance for more than one channel to break through. Based on the behaviour simulated in several random field realizations, two out of ten realizations for the  $\sigma/\mu = 0.1$  case had two

channels breaking through, while this did not occur in any realizations with the higher values of  $\sigma/\mu$ .

Next we discuss two quantitative attributes that summarize behaviour at the scale of the entire fracture: the flow rate through the fracture (which is also a surrogate for the effective transmissivity) and the rate at which calcite mass is removed. Figure 4 shows the evolution of flow rate through the fracture with time, for all three values of  $\sigma/\mu$ . Initially, the flow rate through the fractures is almost exactly the same, because their hydraulic apertures were equal. The fracture with  $\sigma/\mu = 1.0$  experiences breakthrough (accompanied by a steep increase in flow rate and onset of turbulent flow,  $t = 26.5$  years) first, followed by the  $\sigma/\mu = 0.1$  and the  $\sigma/\mu = 0.5$  cases ( $t = 40.5$  and 41.5 years respectively). The abrupt jumps in the flow rate after breakthrough correspond to times when previously subdominant fingers were connected to the dominant finger (in a sense, they represent ‘breakthrough’ of the subdominant fingers into the dominant finger). The flow rate increases more gradually after turbulent flow sets in, unlike just before the breakthrough time. The cumulative rate of mass removal with time (Figure 4) shows trends similar to the flow rate. In the turbulent flow stage after breakthrough, the mass removal rate is larger than during the early laminar flow stage, but smaller than at breakthrough. In the turbulent flow stage, the mass removal rate exhibits isolated kinks, which are associated with the connection of subdominant channels to the main channel. Some of these peaks correspond directly to the kinks in the flow rate vs time curves.

The above results have focused on a single realization of a variable aperture fracture. In order to ascertain the general features of variation in quantities such as the breakthrough time with  $\sigma/\mu$ , it is useful to consider behaviour in a number of realizations. Simulations were carried out in a total of 10 realizations up to the breakthrough time. The variation of the ensemble average breakthrough time with  $\sigma/\mu$  is shown in Figure 5. The bars around the data points represent  $\pm$  one standard deviation bounds, based on the variability in breakthrough time across the realizations. Although not shown in Figure 5, the breakthrough time in a one-dimensional flow system (or equivalently a fracture with a homogeneous initial aperture field,  $\sigma/\mu = 0$ ) was computed as 1504 years. Compared to a one-dimensional flow system where instabilities and fingered growth cannot be represented, the breakthrough time in variable aperture fractures with two-dimensional features is reduced by more than an order of magnitude. Our simulations indicate that the breakthrough time varies non-monotonically with  $\sigma/\mu$ , although this non-monotonic variation is only minor compared to the dramatic reduction in breakthrough time from that in a one-dimensional flow system. In an overall assessment, we may conclude that heterogeneity plays a significant role in accelerating the rate of increase of effective transmissivity of limestone fractures in the

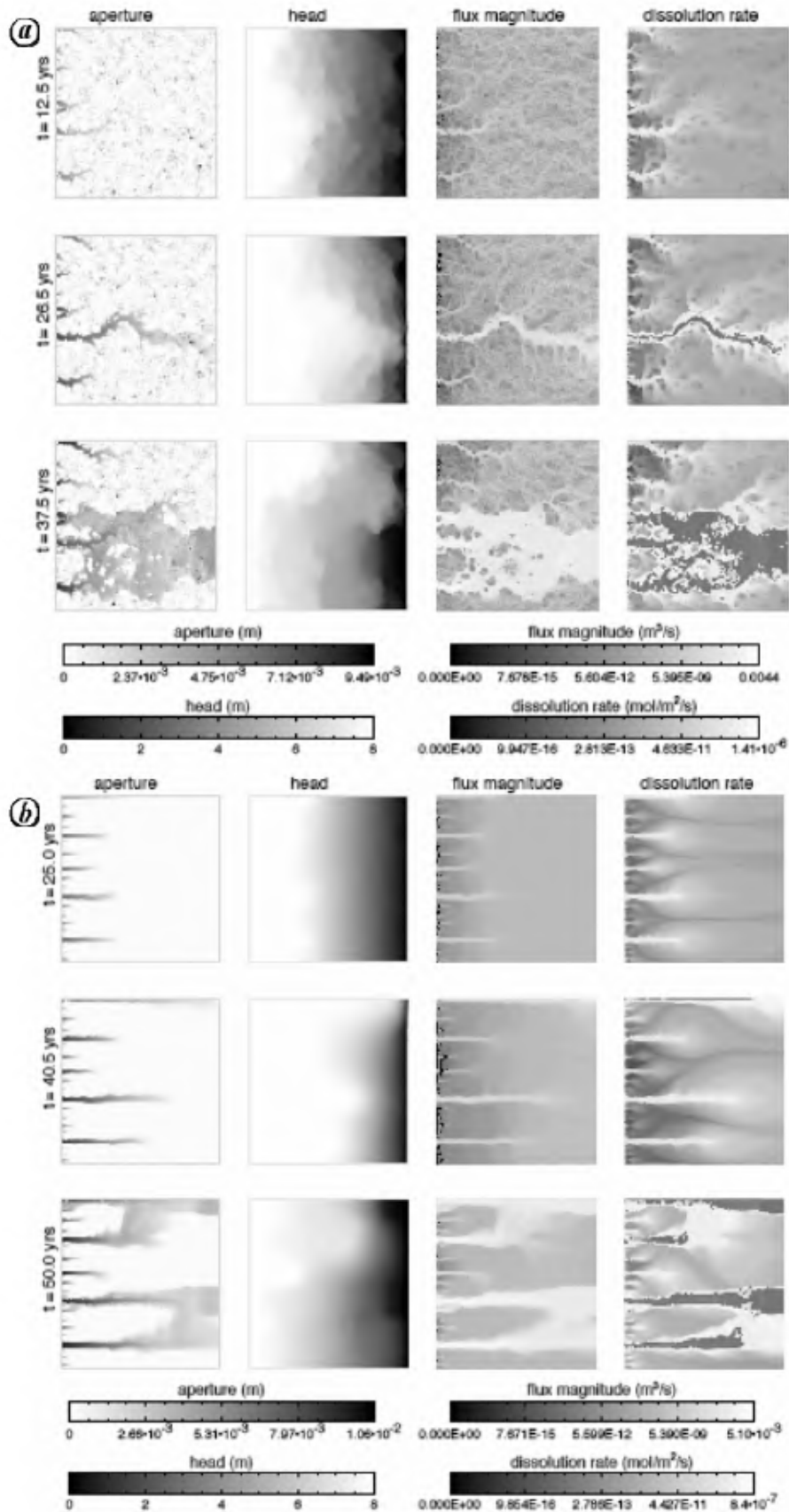


**Figure 3.** Evolution of aperture, head, flux magnitude and dissolution rate fields for meteoric karst evolution simulation with coefficient of variation of the aperture field. *a*,  $\sigma/\mu = 1.0$ ; *b*,  $\sigma/\mu = 0.1$ .

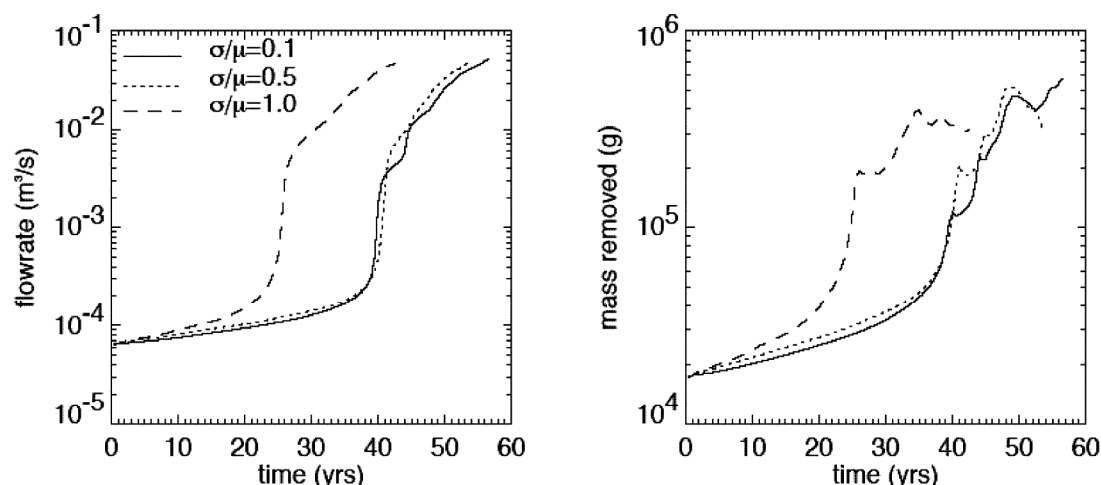


**Figure 4.** Evolution of cumulative flow rate and calcite mass removal rate for the simulations shown in Figures 1 and 3. The kinks in the curves after the breakthrough time correspond to connection of subdominant fingers with the dominant finger.

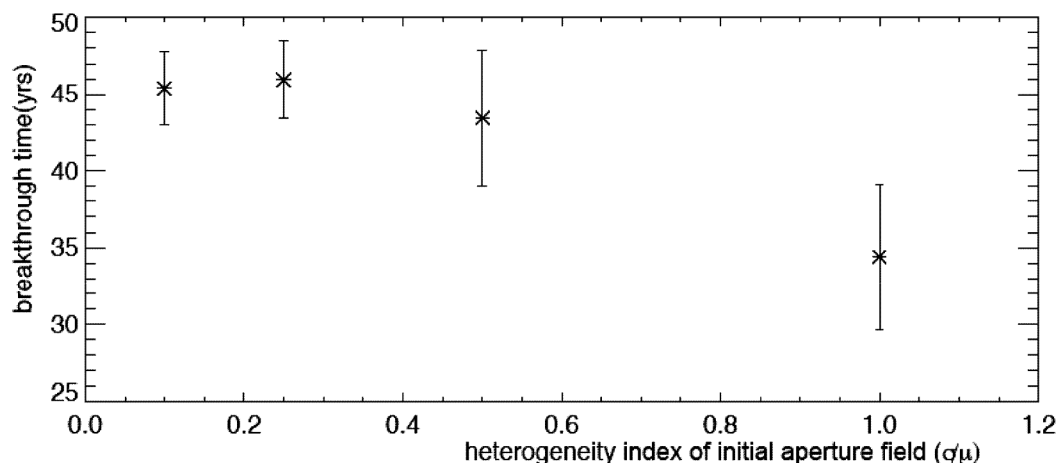


**Figure 5.** Variation of breakthrough time with coefficient of variation of the aperture field ( $\sigma/\mu$ ) in the meteoric case simulations. The bars around the symbols show the one standard-deviation bounds of the variability in breakthrough time among aperture field realizations with the same value of  $\sigma/\mu$ .

meteoric case, although the specific nature of heterogeneity is of secondary importance.

### Hypogene karst simulations

There are relatively fewer reports of previous attempts to model the origin of hypogene caves and karst system evolution in hydrothermal flow systems. Andre and Rajaram<sup>13</sup> presented a multi-component reactive transport model coupled to fluid flow, heat transfer, and aperture growth in a one-dimensional fracture, exchanging heat with a two-dimensional rock mass (i.e. vertical cross-sectional model). They considered upward flow driven by a constant head gradient, with a geothermal gradient maintained constant at some distance from the fracture in the rock mass. Their key conclusion was that it is indeed

possible for conduits to grow significantly over geologically reasonable time-scales. They also made two other important observations: (i) the behaviour during the early stages of development is explained largely based on the retrograde solubility of calcite (i.e. increasing solubility with decreasing temperature along a flow path), without requiring a detailed representation of dissolution kinetics; and (ii) buoyant convective flow via the Rayleigh–Benard type instability could arise in the intermediate and late stages of karstification, and may contribute to the development of maze-work patterns. The first observation greatly facilitates computational tractability, as explained here. The second observation suggests that computational models of this problem would be incomplete if they do not account for buoyancy-driven flow, hence demanding a multi-dimensional representation of the flow system to allow convection rolls. Chaudhuri *et al.*<sup>17</sup> revisited the

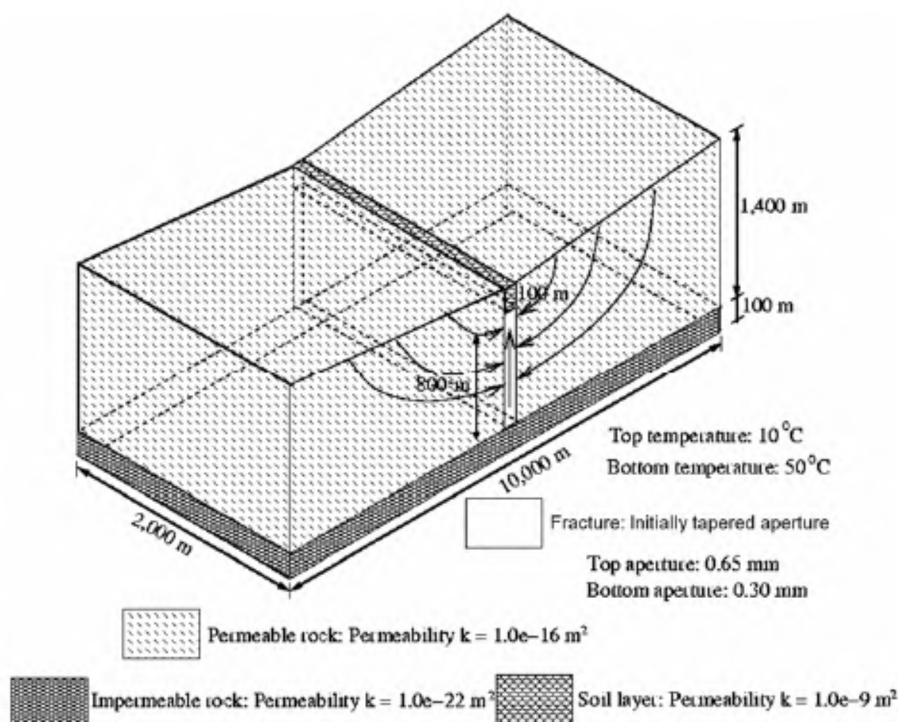


**Figure 6.** Geometry and dimensions for the simulations of hypogene karst evolution in a mountain hydrologic system. The top surface schematically shows the prescribed water table (1400 m above the impermeable rock layer at the outer boundaries, and 900 m above the impermeable rock layer in the centre, with a linear increase away from the centre on both sides).

problem using such a multi-dimensional approach. They confirmed most of the early-time behaviour observed by Andre and Rajaram<sup>13</sup>, and showed further that buoyant convection is indeed initiated when the fracture permeability is increased beyond a certain value. Both the aforementioned studies considered a vertical fracture with constant pressure boundary conditions (greater than hydrostatic pressure at the bottom to drive upward flow).

In this section, we expand the above investigations to consider fracture dissolution in a mountain hydrologic system, wherein a water table provides the driving head for upward flow. This is a more realistic setting than the constant pressure boundary conditions imposed at the top and bottom of the fracture in previous work. Figure 6 shows a schematic representation of the flow system. In the mountain hydrologic system, the presence of the low-permeability layer at depth creates an initial flow pattern where flow lines descend from the water table through the upper rock unit and flow out upwards through the fracture (to springs or other surface discharges). The boundary conditions for the flow are set up with a water table rising from the fracture at a constant slope of 0.1 on top and an impermeable boundary at the bottom. A steady-state water table condition is imposed for this simulation. In future work, we will use a specified recharge rate and allow the water table elevation to be transient in response to the evolving fracture permeability. The thermal boundary conditions for the problem are

imposed as a linear temperature variation from 50°C at the bottom to 10°C at the top at the outer edges of the rock, to represent a geothermal gradient. There is some subtlety involved in specifying the boundary conditions at the top of the fracture zone. A soil layer is defined at the top of the fracture, where permeability is not altered. The boundary conditions for the heat transport problem at the top of the soil layer are set up so that downwelling water has a temperature of 10°C, and upwelling water flows out at the computed boundary temperature (i.e. there is no conductive flux out of the domain in these regions).

#### *Modifications to the general flow and transport equations*

The main modifications to the general flow and transport equations for the hypogene problem are outlined below. We used a different and more recent form for the turbulent resistance law<sup>31</sup>, which provides a smoother transition over a range of Reynolds number:

$$f(\text{Re}) = \frac{1}{1 + 0.00838 \text{Re}} \quad (11)$$

To simulate behaviour in the mountain hydrologic system, it is also necessary to represent flow and heat trans-

port in the rock matrix. The flow equation in the rock matrix is the conventional saturated porous medium flow equation.

$$\frac{\partial(\rho\phi)}{\partial t} + \nabla \cdot (\rho \mathbf{v}_r) = 0, \quad (12)$$

where the porosity  $\phi$  can change with time due to dissolution/precipitation. In eq. (12),  $\mathbf{v}_r$  denotes the Darcy flux vector in the rock matrix. The heat transport equation in the rock matrix is the three-dimensional equation:

$$\frac{\partial(\rho C_{pr} T_r)}{\partial t} + \nabla \cdot (\rho \mathbf{v}_r h_r) - \nabla \cdot (\lambda_r \cdot \nabla T_r) = 0. \quad (13)$$

In eq. (13),  $C_{pr}$  is bulk specific heat and other quantities are as defined previously. In the flow and transport equations for the hypogene system, the density of water ( $\rho$ ) is explicitly represented as a function of temperature ( $T$ ) and pressure ( $p$ ), to simulate buoyancy forces. Additionally, the viscosity ( $\mu$ ) and enthalpy ( $h$ ,  $h_r$ ) are also represented as functions of temperature. The dependence of  $\rho$ ,  $h$ ,  $h_r$  and  $\mu$  on  $T$  and  $p$  are fitted using rational polynomials<sup>32</sup>. Simulation of hypogene karstification involves coupled transient solution of the flow and heat transport equations in the fracture and rock matrix eqs (3), (4), (12), (13).

As noted previously, the evolution of the hypogene karst system is largely controlled by the retrograde solubility of calcite, and there is no need to solve a solute transport equation for  $\text{Ca}^{2+}$ . Instead, we assume that the fluid is locally in equilibrium with calcite everywhere. However, the variation in solubility (due to temperature and/or pressure variations) along a flow path implies a mass flux of  $\text{Ca}^{2+}$ , which balances the source term from calcite dissolution and inflow from the rock matrix ( $R_C$ ) to conserve mass. Chaudhuri *et al.*<sup>15</sup> showed that the mass flux of  $\text{Ca}^{2+}$  is dominated by the advective flux, and the diffusive/dispersive fluxes can be neglected. Thus the rate of aperture alteration can be expressed from eq. (5) as:

$$\frac{\partial b}{\partial t} = \frac{\nabla \cdot (\mathbf{q} C_s(T, p))}{\omega \rho_f}. \quad (14)$$

For use in eq. (10), the solubility of calcite ( $C_s$ ) needs to be specified as a function of temperature and/or pressure. This function is defined as:

$$C_s(T, p) = (1 + 0.0024(p - p_0)) \times (1.42 \times 10^{-3} - 1.97 \times 10^{-4}T - 4 \times 10^{-8}T^2), \quad (15)$$

where  $p_0$  is a reference pressure, and  $T$  is in degrees C. Note that the  $C_s$  decreases with temperature. An important difference between the simulation of the meteoric

system from the previous section and the hypogene system is that there is no finger formation, propagation or competition. The rate of alteration can be computed from eq. (14) and coupled explicitly to the flow and heat transport equations. Yet, it is evident from eq. (14) that preferential flow paths (higher flux) will grow at a faster rate all along their length in the early stages of karstification, when the solubility gradient is more or less uniform in space and potentially lead to pattern formation. As we will see later, buoyant convection provides another mechanism for pattern formation.

## Computational results

In this section, we present two sets of simulations to illustrate the evolution of hypogene karst in a mountain hydrologic system. The geological context for the problem could involve exhumation of a limestone unit with a long vertical fracture/fault, resulting in the formation of a water table and a deep-circulating flow system. Karstification is enabled by upward flow, which causes increased solubility and thus sustains dissolution along a flow path within the fracture. In the first simulation, we consider a fracture with an initial aperture that varies only with height from 0.3 mm at the bottom to 0.65 mm at the top (such a variation is consistent with the greater lithostatic stresses at depth). There are no aperture variations in the  $x$ -direction initially. Figure 7 shows the evolution of the aperture, temperature and flux fields in the fracture through time. Initially, the water flux in the fracture is upward (with no  $x$ -variation) in the entire fracture. The upward flux increases with height ( $z$ ), due to lateral inflow from the rock. The temperature also does not vary with  $x$ , and the variation with  $z$  is almost linear, because the lateral inflow negates the influence of forced convective effects. The aperture growth rate will be larger at higher  $z$ , because of the increased water flux (see eq. (14)). At  $t = 24,953$  years (Figure 7 a2, b2 and c2), the aperture and effective transmissivity have grown large enough to lead to buoyant convective flow cells (Figure 7 c2), and the aperture, temperature and flow fields start to exhibit variations in the  $x$ -direction. In this particular case, we see 6 convection rolls; and in other simulations, we have seen 4–8 convection rolls. The temperature field shows higher temperatures in upward flow paths, but there is still a temperature gradient sustaining dissolution growth in these regions. In the downward flow regions, precipitation occurs (because solubility decreases along the flow direction). Because the overall effective transmissivity of the system (rock + fracture) does not increase significantly, the total upward water flux integrated over any horizontal section of the fracture does not change significantly with time. To satisfy this constraint, the upward flow zones where the transmissivity increases become narrower with time, and the downward flow zones where

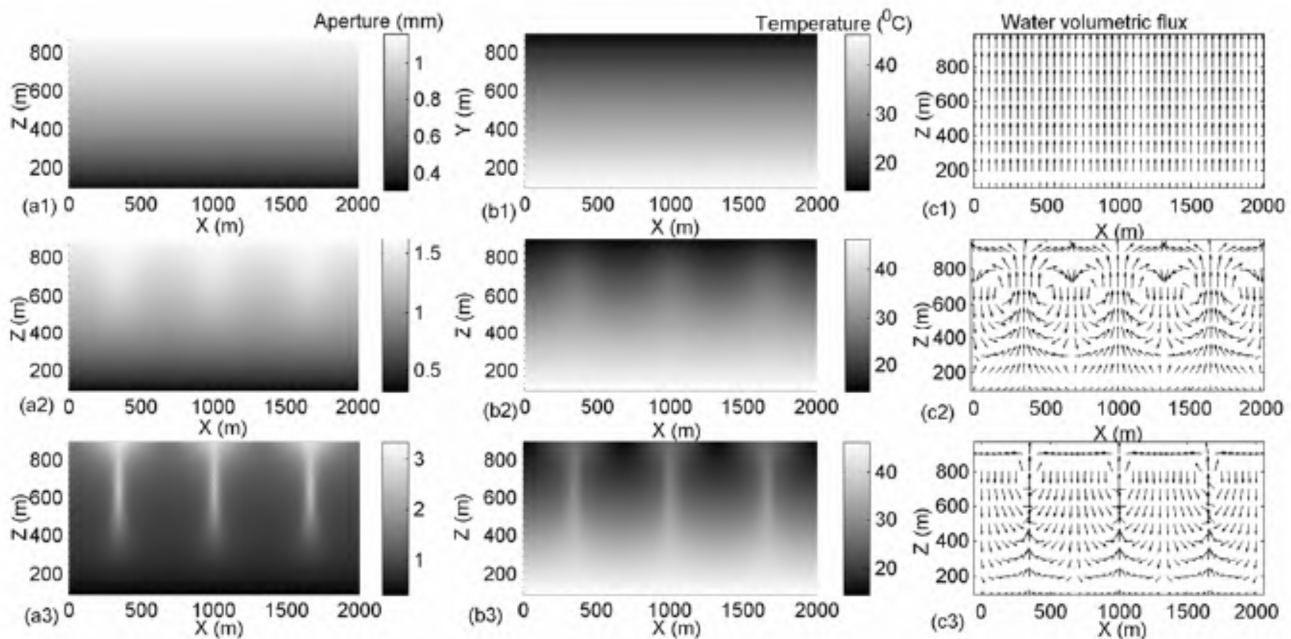


**Figure 7.** Evolution of aperture, temperature and volumetric flux fields (magnitude is in log scale) at three different times for hypogene karst evolution simulation in an initially homogeneous aperture field: (a1–c1) at conductive-forced convective regime,  $t = 13,446$  years, (a2–c2) just after the onset of buoyant convection,  $t = 24,953$  years, and (a3–c3) final configuration with narrow upward flow channels,  $t = 26,412$  years.

transmissivity decreases become wider (compare Figure 7 a2 and 7 a3). This flow configuration remains stable for a long duration. Thus, this simulation shows how the phenomenon of buoyant convection can lead to a regular pattern of dissolution channels sustaining upward flow, even in a system where the total hydrologic flux remains more or less constant, due to the constraints imposed by the low rock permeability. Note that in contrast with the meteoric system, the dissolution channels are formed largely near the outflow boundary and not from the inflow boundary.

In the second simulation, we consider a variable-aperture fracture defined by perturbing the linear aperture variation in the first simulation with a zero-mean isotropic stationary random field (log-normal, with a standard deviation of  $\log\text{-aperture} = 0.1$ , and a Gaussian correlation function with a correlation length of 170 m). The flow field at 10,706 years (Figure 8 c1) shows preferential flow channels along which the aperture has enlarged preferentially because of the larger water flux (see eq. (14)). Similar behaviour was noted by Andre and Rajaram<sup>13</sup> and Chaudhuri *et al.*<sup>15</sup>. At the same time, there is also a general (albeit smaller) increase in the aperture over large regions of the fracture due to the upward flow. When the effective transmissivity exceeds a threshold, buoyant convection rolls are formed ( $t = 15,672$  years, see the downward flow regions in Figure 8 c2). With time, it appears that the preferential flow channels form a template as the up-flow channels in the buoyant convective flow pattern. Otherwise, the overall behaviour is not very much different from that of the first simulation, except that in this case, the dissolution channels sustaining

upward flow were formed before the onset of buoyant convection, and there is an earlier onset of buoyant convection. In terms of time scales, it is useful to point out that the time required for the onset of buoyant convection in the mountain hydrologic system is longer by a factor of 2–5 compared with similar simulations that were based on constant pressure boundary conditions imposed at the ends of the fracture alone<sup>17</sup>. This is largely because the flow rate through the system is restricted by the low permeability of the rock matrix that flow has to pass through.

Although we see the development of a pattern of up-flow channels in both simulations, we have not successfully produced a maze-like network. This leads to several questions about the mode of origin of maze networks. We first note that it is plausible that with different degrees of heterogeneity (and spatial correlation lengths) in the fracture aperture, preferential flow channels formed at intermediate times (e.g. as in Figure 8 a1) dominate the behaviour and buoyant convection never occurs. If we take a multiscale view of the geological system represented at the kilometre scale in Figure 6, the rock mass itself may be fractured, with a greater intensity of fracturing near the fracture/fault plane. If we now consider a dissolution channel that forms due to upward flow through a network of smaller fractures with lengths of the order of 10–100 m, one can imagine how such a network can be uniformly enlarged to form a maze (the key point is that unlike in the meteoric case, where there is finger competition, there is no mechanism to prevent dissolution of multiple branches of a flow path in the hypogene case). It is interesting to note that conditions for the



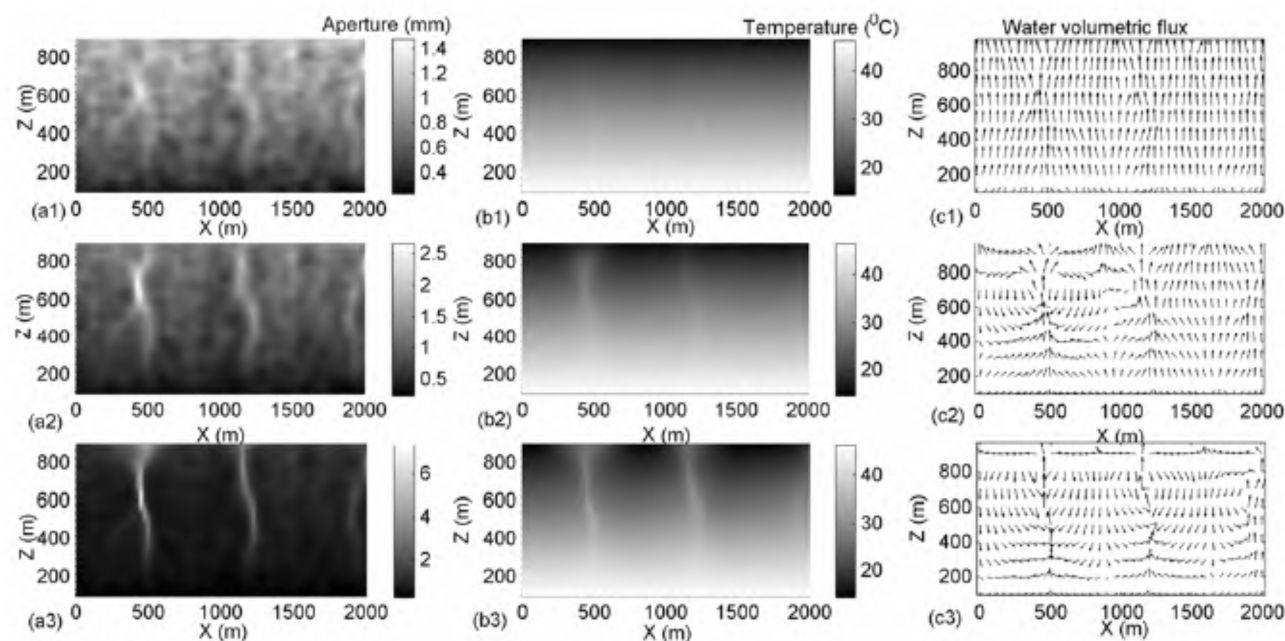


**Figure 8.** Evolution of aperture, temperature and volumetric flux fields (magnitude is in log scale) at three different times for hypogene karst evolution simulation in an initially heterogeneous aperture field: (a1–c1) at conductive-forced convective regime,  $t = 10,706$  years, (a2–c2) just after the onset of buoyant convection,  $t = 15,672$  years, and (a3–c3) final configuration with narrow upward flow channels,  $t = 18,138$  years.

formation of such a maze can occur either due to preferential flow resulting from heterogeneous initial aperture, or by buoyant convective flow, which leads to discrete upflow channels. These up-flow channels could also lead to hot spring discharges that are known to occur in hypogene karst systems, including the famous thermal springs at Bath, England<sup>13,33</sup>, which are more common than hypogene caves.

### Discussion: what did we learn about karst evolution and how is it relevant to engineered systems?

First, we should note that ‘caves’ are large enough for humans to walk in, sometimes incorporating room-size passages. Clearly, there are a lot of late-stage processes involved in these transformations (e.g. transition from aperture-filling to open channel flow and potential descent of channels) that are beyond the reach of our modelling approaches. However, our simulations of the meteoric system indeed demonstrate the early stages of the formation of a branchwork pattern, consistent with observations of meteoric karst systems. Future work will focus on modelling the transition to open channel flow and subsequent evolution of cave passages. It may be expected that after open channel flow is initiated, the lower portion of the conduit will continue to dissolve and there will be a stage of passage enlargement by downcutting. As noted above, we did not really demonstrate the development of a maze network in the hypogene case simulations. Indeed, we cannot successfully reproduce three-dimensional maze-like structures without advanced

computations of coupled processes in three-dimensional fracture networks. Nevertheless, the simulations presented here are highly illuminating, in that they show how dissolution (and hence karstification) can be sustained along upflow paths resulting from either buoyant convection and/or preferential flow, thus establishing ideal environments for hypogene cave formation. It is also encouraging that our simulation results are able to distinguish between salient aspects of meteoric and hypogene karst evolution. Simulations of coupled processes in large three-dimensional discrete fracture networks are beyond the capabilities of the coupled process simulators of today. Modern parallel computing combined with innovative ideas on multiscale modelling hold promise in the context of future work on this problem, and it will serve as a useful test-case for demonstrating the fidelity of the next generation of high-performance coupled process codes.

As we stated in the first section, simulations of coupled processes in geological systems can yield useful insights on dominant phenomena and guide the development of simplified, efficient models for engineered earth systems. We now elaborate further on this theme. In our view, there are three important elements that can be distilled from our investigations of karst evolution, relating to: (i) the importance of fractures to flow and transport processes in rock masses, (ii) the role of heterogeneity in the context of coupled processes in complex earth systems and (iii) the limits to ‘predictability’ in engineered earth systems, and consequences for design and operation.

In low-permeability rock masses, fractures occupy a very small volume fraction, but dominate the overall

behaviour of transport processes. Thus, tracking the evolution of fracture properties is important; note that the fracture transmissivity has a very sensitive (cubic) dependence on aperture. The results in the two previous sections clearly suggest that the dominant consequences of coupled-process interactions may be completely missed if we use an equivalent porous medium model rather than a fracture-based conceptual model. We believe that there is a strong case for building useful fracture-based conceptual models to predict the response of rock masses to engineered perturbations. Although the field of rock mechanics has investigated mechanical perturbations in detail, several of the engineering problems mentioned in the introduction require investigation of coupled processes. In general the properties of fractures and fracture networks are controlled by interactions between hydraulic (pressure-dependent aperture), mechanical (deformation and fracturing), thermal (expansion/contraction of rock) and chemical (dissolution/precipitation) processes. Discrete fracture network models for understanding the response of fractures (the primary transport pathways in low-permeability rock) to engineered perturbations are still under development<sup>7</sup>, and will be greatly aided by advances in high-performance computational technology.

The substantial literature on stochastic subsurface hydrology<sup>34</sup> examines the influence of the ubiquitous heterogeneity in properties of natural earth materials on flow and transport, proposing elegant theoretical relationships for macrodispersion coefficients and effective transmissivities. This body of literature has also provided us with a humbling perspective on the uncertainties involved in modelling subsurface flow and transport. At first glance, the whole enterprise of coupled-process simulations for predicting the behaviour of complex earth systems may appear daunting in the light of heterogeneity and uncertainty. Yet, there is a certain robustness in the consequences of nonlinear interacting processes investigated here, which transcends the detailed representation of heterogeneity, and seems to be a result of self-organization inherent in the coupled interactions. For instance, in the meteoric karst simulations, the differences in behaviour across the three different  $\sigma/\mu$  cases considered are of secondary importance – in all cases, a single dominant finger emerges, and the variation of the breakthrough time with  $\sigma/\mu$  is insignificant compared to the difference from an idealized parallel-plate fracture. The dominant behaviour (breakthrough of a single or occasionally multiple fingers) is fundamentally the same for any realization of the initial aperture field. The behaviour after turbulence is also similar; furthermore this behaviour is relatively insensitive to details of how turbulent resistance is represented.

Thus the investigation of the meteoric karst evolution provides us with useful insights about the behaviour of related engineered systems where fracture dissolution

results from interaction between relatively fresh solutions and rock minerals (e.g. leakage of dams through underlying gypsum or limestone formations<sup>35</sup>; injection of CO<sub>2</sub>, which leads to carbonated solutions<sup>3</sup>; acid injection to improve efficiency for oil recovery<sup>36</sup>). In all these cases, formation of dissolution fingers is probably the robust dominant behaviour, and their influence should be considered in design/operation. We may never be able to precisely predict *a priori* the paths followed by dominant dissolution channels even with extensive site characterization. A better alternative may be to proceed with the understanding that fingers are bound to form, and (a) make design modifications (e.g. grout fractures) that will restrict their growth or (b) design monitoring schemes that can locate fingers after they form (but before it is too late) and control their propagation. It is plausible that in some cases, the engineering operations (a) and (b) are simply impractical. In such cases, the engineering decision making process should acknowledge that ‘runaway’ fingers are the dominant feature of these systems and accept the risk associated with the inability to pinpoint the location of these fingers. Based on our modelling results, we believe that for a given set of conditions, it should be possible to at least estimate finger velocities and other relevant properties of fingers based on a combination of Monte-Carlo simulations and theoretical analyses, which would greatly aid in quantifying the probability of runaway growth over a given time horizon.

Similar comments apply in the case of systems with significant thermal perturbations (e.g. nuclear waste repositories). Andre and Rajaram<sup>13</sup> and Chaudhuri *et al.*<sup>17</sup> showed that there is a long dormant phase followed by a rapid jump in the flow rate through fractures experiencing growth by dissolution under certain conditions. Our simulations in the previous section also suggest that the onset of buoyant convection happens relatively abruptly, when the effective transmissivity of the fracture crossed a threshold value. It is thus important in these cases to properly account for density gradients and constrain the time scales associated with various critical transformations in system behaviour. Although, we have not considered examples where precipitation is the dominant process, similar arguments can be made in the context of permeability reduction by precipitation, which may be beneficial for instance in the context of forming a barrier against solute or radionuclide transport, or a hindrance in the case of scale formation in geothermal energy systems. Chaudhuri *et al.*<sup>15</sup> recently presented an analysis suggesting the tendency for the formation of precipitate bodies aligned perpendicular to flow in a variable-aperture fracture, which is favourable from the viewpoint of containment, but unfavorable in terms of maintaining permeability.

In conclusion, we believe that much can be learned from testing coupled process simulators for engineered earth systems against natural analogs. The ability to reproduce important natural phenomena even qualitatively

will greatly strengthen our confidence in applying these simulators as analysis tools for evaluating the long-term behaviour of earth systems subjected to significant human perturbations. We have only presented a small and simple subset of such systems here. There is a large class of interesting problems involving thermal, hydrologic, mechanical and chemical (THMC) interactions<sup>6</sup> that are increasingly coming within the reach of modern high-performance computation. Careful simulations accounting for the role of fractures can yield useful insights on the dominant behaviours emerging from these interactions, and guide engineering design, operations and risk analysis.

1. United States Department of Energy, Radioactive waste: an international concern, Fact Sheet, Office of Civilian Radioactive Waste Management, 2001; <http://www.ocrwm.doe.gov/factsheets/doevmp0405.shtml>
2. Metz, B. and Davidson, O. (eds), IPCC. *Climate Change 2007 Mitigation*, Contribution of Working Group III to the Fourth Assessment Report of the Intergovernmental Panel on Climate Change. Cambridge University Press, Cambridge, 2007.
3. Metz, B., Davidson, O., de Coninck, H. C., Loos, M. and Meyer, L. A. (eds), IPCC, *IPCC Special Report on Carbon Dioxide Capture and Storage*, Prepared by Working Group III of the Intergovernmental Panel on Climate Change. Cambridge University Press, Cambridge, 2005.
4. Armstead, H. C. H., *Geothermal Energy, Its Past, Present and Future Contributions to the Energy Needs of Man*, E. & F. N. Spon Ltd, London, New York, 1983.
5. MIT, The Future of Geothermal Energy. Impact of Enhanced Geothermal Systems (EGS) on the United States in the 21st Century, Assessment by a Massachusetts Institute of Technology led panel (J. F. Tester, Chair), 2006; [http://geothermal.inel.gov/publications/future\\_of\\_geothermal\\_energy.pdf](http://geothermal.inel.gov/publications/future_of_geothermal_energy.pdf)
6. Tsang, C. F. (ed.), *Coupled Processes Associated With Nuclear Waste Repositories*, Academic Press, Inc, Orlando, Florida, 1987.
7. Stephansson, O., Hudson, J. A. and Jing, L., *Coupled thermo-hydro-mechanical-chemical processes in geo-systems [electronic resource]: fundamentals, modelling, experiments and applications*, Elsevier, Amsterdam, Boston, 2004.
8. Palmer, A. N., Origin and morphology of limestone caves. *Geol. Soc. Am. Bull.*, 1991, **103**, 1–21.
9. Ford, D. C. and Williams, P. W., *Karst Geomorphology and Hydrology*, CRC Press, Boca Raton, Florida, 1989.
10. Ortoleva, P., *Geochemical Self-Organization*, Oxford University Press, Oxford, 1994.
11. Ingebritsen, S. E. and Rojstaczer, S. A., Controls on geyser periodicity. *Science*, 1993, **262**, 889–892.
12. Nadeau, R. M. and McEvilly, T. V., Fault slip rates at depth from recurrence intervals of repeating microearthquakes. *Science*, 1999, **285**, 718–721.
13. Andre, B. J. and Rajaram, H., Dissolution of limestone fractures by cooling waters: early development of hypogene karst systems. *Water Resour. Res.*, 2005, **41**, W01015.
14. Dreybrodt, W., Principles of early development of karst conduits under natural and man-made conditions revealed by mathematical analysis of numerical models. *Water Resour. Res.*, 1996, **32**, 2923–2935.
15. Chaudhuri, A., Rajaram, H. and Viswanathan, H., Alteration of fractures by precipitation and dissolution in gradient reaction environments: computational results and stochastic analysis. *Water Resour. Res.*, 2008, **44**, W10410.
16. Hanna, R. B. and Rajaram, H., Influence of aperture variability on dissolutional growth of fissures in karst formations. *Water Resour. Res.*, 1998, **34**, 2843–2853.
17. Chaudhuri, A., Rajaram, H., Viswanathan, H., Zyvoloski, G. and Stauffer, F., Buoyant convection resulting from dissolution and permeability growth in vertical limestone fractures. *Geophys. Res. Lett.*, 2009, **36**, L03401 (in press).
18. Siemers, J. and Dreybrodt, W., Early development of karst aquifers on percolation networks of fractures in limestone. *Water Resour. Res.*, 1998, **34**, 409–419.
19. Groves, C. G. and Howard, A. D., Minimum hydrochemical conditions allowing limestone cave development. *Water Resour. Res.*, 1994, **30**, 607–615.
20. Groves, C. G. and Howard, A. D., Early development of karst systems: 1. Preferential flow path enlargement under laminar flow. *Water Resour. Res.*, 1994, **30**, 2837–2846.
21. Clemens, T., Huckinhaus, D., Sauter, M., Liedl, R. and Teusch, G., A combined continuum and discrete network reactive transport model for the simulation of karst development, calibration and reliability in groundwater modeling. Proceedings of the MODEL CARE 96 Conference held at Golden, CO, USA, USAGS Pub. No. 237, September 1996.
22. Kaufmann, G. and Braun, J., Karst aquifer evolution in fractured rocks. *Water Resour. Res.*, 1999, **35**, 3223–3238.
23. Louis, C., A study of groundwater flow in jointed rock and its influence on the stability of rock masses, Imperial College Rock Mechanics Research Report No. 10, 1969.
24. Cheung, W., Towards a better understanding of fissure growth in karst formations: investigations from genesis to maturation and the influence of fracture-matrix interactions, Ph D thesis, University of Colorado, Boulder, 2002.
25. Shah, R. K. and London, A. L., *Laminar Flow Forced Convection in Ducts: A Source Book for Compact Heat Exchange Analytical Data*, Academic Press, San Diego, 1978.
26. Gnielinski, V., New equations for heat and mass transfer in turbulent pipe and channel flow. *Int. Chem. Eng.*, 1976, **16**, 359–368.
27. Howard, A. D. and Groves, C. G., Early development of karst systems: 2. Turbulent flow. *Water Resour. Res.*, 1995, **31**, 19–26.
28. Ewers, R. O., Cavern development in the dimensions of length and breadth, Ph D thesis, McMaster Univ., Hamilton, Ontario, Canada, 1982.
29. Cheung, W. and Rajaram, H., Dissolution finger growth in variable fractures: role of the tip-region flow field. *Geophys. Res. Lett.*, 2002, **29**, 2075.
30. Szymczak, P. and Ladd, A. J. C., A network model of channel competition in fracture dissolution. *Geophys. Res. Lett.*, 2006, **33**, L05401.
31. Zimmerman, R. W., Al-Yaarubi, A., Pain, C. C. and Grattoni, C. A., Nonlinear regimes of fluid flow in rock fractures. *Int. J. Rock Mech. Min. Sci.*, 2004, **41**, 384.
32. Zyvoloski, G., FEHM: a control volume finite element code for simulating subsurface multi-phase multi-fluid heat and mass transfer, LAUR-07-3359, Los Alamos National Laboratory, 2007; <http://fehm.lanl.gov/>
33. Worthington, S. R. H., Karst hydrogeology of the Canadian Rocky Mountains, Ph D thesis, McMaster Univ., Hamilton, Ontario, Canada, 1991.
34. Gelhar, L. W., *Stochastic Subsurface Hydrology*, Prentice-Hall, Upper Saddle River, NJ, 1993.
35. James, A. N. and Lupton, A. R. R., Gypsum and anhydrite in foundation of hydraulic structures. *Geotechnique*, 1978, **28**(3), 249–272.
36. Daccord, G., *Carbonate Acidizing: Toward A Quantitative Model of the Wormholing Phenomenon*, Society of Petroleum Engineers, 1989, pp. 63–68.

ACKNOWLEDGEMENT. This research was supported by grants from the National Science Foundation (EAR973404) and the Institute for Geophysics and Planetary Physics (1714-07).